Received: 18 February 2016 | Revised: 6 June 2016 | Accepted: 2 July 2016

DOI: 10.1002/cnm.2821

WILEY

CMBE15: SELECTED PAPERS FROM THE 4TH INTERNATIONAL CONFERENCE ON COMPUTATIONAL & MATHEMATICAL BIOMEDICAL ENGINEERING 2015

A comparison of hemodynamic metrics and intraluminal thrombus burden in a common iliac artery aneurysm

Lachlan J. Kelsey[1,2] | Janet T. Powell[3] | Paul E. Norman[1,4] | Karol Miller[2,5] | Barry J. Doyle[1,6,7]

[1] Vascular Engineering Laboratory, Harry Perkins Institute of Medical Research, Perth, WA, Australia

[2] Intelligent Systems for Medicine Laboratory, School of Mechanical and Chemical Engineering, The University of Western Australia, Crawley, WA, Australia

[3] Vascular Surgery Research Group, Imperial College London, London, UK

[4] School of Surgery, The University of Western Australia, Crawley, WA, Australia

[5] Institute of Mechanics and Advanced Materials, Cardiff University, Cardiff, UK

[6] School of Mechanical and Chemical Engineering, The University of Western Australia, Crawley, WA, Australia

[7] British Heart Foundation Centre for Cardiovascular Science, The University of Edinburgh, Edinburgh, UK

Correspondence
Barry J. Doyle, Vascular Engineering Laboratory, Harry Perkins Institute of Medical Research, Perth, WA, Australia.
Email: Barry.Doyle@uwa.edu.au

Abstract

Aneurysms of the common iliac artery (CIAA) are typically found in association with an abdominal aortic aneurysm (AAA). Isolated CIAAs, in the absence of an AAA, are uncommon. Similar to AAAs, CIAA may develop intraluminal thrombus (ILT). As isolated CIAAs have a contralateral common iliac artery for comparison, they provide an opportunity to study the hemodynamic mechanisms behind ILT formation.

In this study, we compared a large isolated CIAA and the contralateral iliac artery using computational fluid dynamics to determine if hemodynamic metrics correlate with the location of ILT. We performed a comprehensive computational fluid dynamics study and investigated the residence time of platelets and monocytes, velocity fields, time-averaged wall shear stress, oscillatory shear index, and endothelial cell activation potential. We then correlated these data to ILT burden determined with computed tomography.

We found that high cell residence times, low time-averaged wall shear stress, high oscillatory shear index, and high endothelial cell activation potential all correlate with regions of ILT development. Our results show agreement with previous hypotheses of thrombus formation in AAA and provide insights into the computational hemodynamics of iliac artery aneurysms.

KEYWORDS

computational fluid dynamics, iliac aneurysm, intraluminal thrombus, wall shear stress

1 | INTRODUCTION

An aneurysm is a localized dilation of an artery that is life threatening when ruptured. Aneurysms of the common iliac artery (CIAA) are most commonly seen in association with an abdominal aortic aneurysm (AAA). Recent large-scale population screening studies show that, for men aged 65 years, the prevalence of an AAA is approximately 2%.[1] In 25% of these cases, there are co-existent aneurysms in 1 or both common iliac arteries, and in 7% of these cases, aneurysms also exist in the internal iliac arteries.[2] The true prevalence of isolated CIAAs is unclear. The underlying causes of most aneurysms in these medium-to-large arteries are unknown and specific pathological or genetic causes are generally only identified in a small number of cases.[3] With respect to CIAAs there is no strong evidence base for their management and the threshold diameter for intervention is often when the diameter exceeds 3.5 to 4 cm[4] or based solely on clinical opinion. Healthy common iliac arteries typically have diameters of approximately 1 to 1.5 cm.[2] Figure 1 shows the healthy anatomy of the iliac artery region compared to an aneurysmal case.

In the past decades, computational fluid dynamics (CFD) has emerged as a powerful and popular tool for the study of

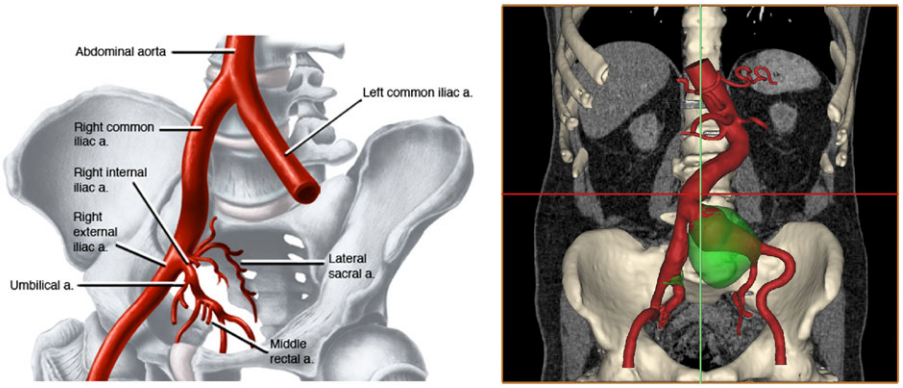

FIGURE 1 A diagram of normal pelvic vasculature[72] (left) aside the coronal view of the patient's 3-dimensional vasculature—reconstructed from computed tomography (right). The patient's artery lumen is in red and thrombus in green. The patient's left common iliac artery aneurysm had a maximum diameter of 8.4 cm (5.7-cm lumen diameter) and right common iliac artery diameter of 3.4 cm (2.6-cm lumen diameter). (a. = artery)

blood flow dynamics of aneurysms and other cardiovascular disease.[5–8] With appropriate boundary conditions and model assumptions, CFD can simulate the blood flow through any vessel of the body using patient-specific geometries, typically derived from computed tomography (CT). To date, much attention has been focused on the study of hemodynamics in AAA yet very little to the computational modelling and assessment of CIAA. When compared with the recent progress of computationally aided assessment of AAA rupture risk[9–11] and other cardiovascular disease,[12–15] there is a need to improve our ability to assess the risk of CIAA. CIAA occurs in some computational models of AAA,[16] although they were not the primary focus of that research. The authors are only aware of 1 other study primarily concerned with the hemodynamics of CIAA,[17] and this work intends to provide more momentum to this topic.

Intraluminal thrombus (ILT) is found in over 70% of clinically relevant AAA.[5,18] In some structural studies, ILT is thought to be beneficial as it may dampen the pressure-wave impact on the wall of AAA and, therefore, potentially reducing the chance of rupture. However, in stark contrast, other studies show that ILT increases rupture risk as it is a potential source of proteolytic activity and an accelerated inflammatory response, tied to local wall thinning, weakening, and hypoxia.[19–21] The direct relationship between ILT and AAA volume is supporting evidence for this latter theory.[20,22,23] Furthermore, the onset and growth of ILT is a continuous process that involves a large number of hemodynamic and biochemical stimuli including the clotting of platelets and other particles.[20,22–24]

Intraluminal thrombus morphology ranges from a structured, layered material, to a homogenous fluid-like structure[25]; at a specific state of maturity, ILT becomes a poroelastic material, whereby its porous structure influences fluid transport from the lumen to the underlying tissue.[7] However, this behavior is not accounted for in rigid wall CFD studies. This is primarily due to variability of ILT mechanical properties[7,25] and the necessity of magnetic resonance imaging to properly view/understand ILT structure.[26] Despite the uncertainty this brings to existing fluid models, the relationship among hemodynamic indices, artery inflammation, and thrombotic susceptibility is continually explored.

Initially, the hemodynamic study of idealized AAA geometries illustrated how the detachment of flow occurs and develops in enlarging aneurysms,[27–29] where this behavior is characterized by localized regions of low and oscillatory wall shear stress (WSS). These observations are physically similar to the separation of the boundary-layer downstream of stenoses, where Raz *et al*[30] showed the direct relationship between platelet recirculation time and both platelet activation and acetylated thrombin generation. Furthermore, Rayz *et al*[31] observed thrombus deposition in certain regions of patient-specific intracranial geometries with an increase in residence time and low WSS. More recently, Boyd *et al* found that AAA rupture tended to occur in thrombus afflicted regions with predicted flow recirculation and low WSS.[32] In addition, it has been shown that regions of low, oscillatory WSS provide a well-described mechanical stimulus that promotes the inflammatory process by inducing an oxidative response in endothelial vascular cells.[33] As a means to quantify this behavior in transient simulations of blood flow, the time-averaged wall shear stress (TAWSS) and the oscillatory shear index (OSI)[34] are often used to measure the interaction between the flow field and the artery wall.[5,35–38] Doyle *et al* showed, via a serial CFD study of a patient-specific AAA over 2.5 years, the direct spatial relationship among low TAWSS, local aneurysm expansion, and localized *in vivo* ILT development.[5] However, it should also be noted that despite thrombotic susceptibility typically being associated with low TAWSS and high OSI, O'Rourke *et al*[37] and Arzani *et al*[38] identified that regions of low OSI had a good correlation with the site specificity of ILT within aneurysms.

Furthermore, the morphology of AAA and the hemodynamic behavior it induces have also been shown to exhibit an activated state of coagulation and fibrinolysis.[39] Biasetti *et al*[40] postulated that platelets are activated as they enter into an aneurysm, where they are enveloped by vortices produced

at the neck and later become entrapped in recirculation zones. Platelets then preferentially attach to preexisting ILT or to the distal regions of the vessel (AAA). This is supported by multiple anatomic studies of ILT, as it commonly occurs in the distal anterior region of AAA.[23,41–43] In 2012, an integrated fluid-chemical approach for modelling ILT formation in AAA was introduced by Biasetti *et al* that showed agreement with the site specificity of ILT formation and the movement of vortex structures.[44]

In addition, Basciano *et al*[45] assessed the residence times and surface-shear loads of platelets and white bloods cells in a patient-specific AAA sac using Eulerian-Lagrangian CFD simulation methodology to investigate the onset of ILT, supporting Biasetti's work and the generalized view that aneurysms entrap blood particles. The 1-way Lagrangian methodology used by Basciano[45] implements a particle drag force, pressure gradient force, and gravity force, to calculate the particle trajectories in the arterial flow field, as these forces are thought to provide a reasonable prediction of cell transport.

The gravity force may be ignored for particles where the fluid-to-particle density ratio is close to unity.[46] Furthermore, when the particle distance from the wall approaches the same order of magnitude as the particle diameter, the typical lift and drag equations break down and require modification to accurately resolve the particle behavior in the "near-wall" region.[46,47] Hardman *et al*[47] implemented near-wall-modified lift and drag forces for the discrete Lagrangian phase in a large eddy simulation in both ideal and patient-specific geometries and found that particle residence time (PRT) in aneurysm sacs was greatly increased for sac sizes where the maximum diameter exceeded 1.8 times the inlet diameter, thus proposing a critical size beyond which monocyte infiltration and wall degradation are greatly increased.

Following these previous studies into ILT and AAA, the objective of this study was to determine if/how well hemodynamic stimuli computationally match the areas of ILT development in both the advanced and the early stages of aneurysmal disease in the common iliac arteries. In this study, we investigated the blood flow of a 91-year-old male patient who did not have AAA, but had a large left CIAA with a maximum anterior-posterior diameter of 8.4 cm. The right common iliac artery was 3.4 cm in diameter. ILT was present in both the large left CIAA and the less aneurysmal right common iliac artery.

2 | METHODOLOGY

2.1 | Three-dimensional reconstruction and trimming

Contrast-enhanced CT data (pixel size = 0.82 mm; slice thickness = 1 mm) of a 91-year-old male with a large CIAA were imported into MIMICS v17 (Materialise, Belgium). We reconstructed the lumen into 3-dimensions (3D) and conservatively smoothed the resulting surfaces (see Figure 1) following our previous methods.[5] We extended the inlet surface by 120 mm (determined using Wood's unsteady entrance length method[48]) and each outlet by 10 times the outlet diameter to ensure flow was fully developed entering the supraceliac (SC) aorta and that the outlet boundary conditions did not affect the hemodynamics in the vessels. The resulting reconstruction contained a number of the minor arteries branching from the internal iliac arteries; these minor arteries are often not captured by CT and subsequently neglected in CFD studies of the normal or diseased aortic bifurcation. We now know that these minor downstream branches have little impact on the upstream hemodynamics.[49] The patient also had a "pocket" (pouch-like cavity), recessing off the posterior of the left CIAA lumen, which was expected to produce complex flow.

2.2 | Meshing

We constructed the volume mesh within STAR-CCM+ (v9.04) (CD-adapco Group) using a core polyhedral mesh and a prism-layer mesh in the boundary layer that became progressively refined approaching the wall. The thickness of the prism-layer mesh and the surface size (edge length) were defined relative to the local lumen diameter so that the smaller arteries were well discretized. Any areas that were expected to have rapid changes in velocity (ie, bifurcations) were also subject to refinement. The mesh can be seen in Figure 2.

To be able to determine a sufficient level of (uniform) mesh refinement (number of prism-layers and polyhedra density coefficient), we applied the Grid Convergence Index (GCI)[50,51] to steady-state simulations using the peak systolic flow conditions (ie, peak flow in Figure 4). Figure 3 below shows the grid convergence of inlet pressure, mean WSS across the aneurysm, and velocity probes scattered throughout the geometry. The GCI of all tested variables was below 2%, and as this is considered to be a sufficient minimization of the spatial discretization error,[5] no further mesh refinement was performed. The finest and chosen mesh (see Figure 2) contained 16 prism-layers and had a total mesh-cell count of 5.87 million.

2.3 | Physical assumptions and boundary conditions

The flow is expected to be turbulent within the patient's aorta and aneurysmal regions during late systole; however, it is also expected to largely relaminarize during diastole and early systole.[35] Reynolds-averaged turbulence models may be used to simulate turbulence efficiently on coarse meshes; although there is strong evidence that they are not suitable for pulsatile, relaminarizing flows in cardiovascular research[52,53]. With this in mind, we approximated the blood flow as laminar and considered the blood to be an incompressible fluid with a density of 1050 kg/m^3. The walls of

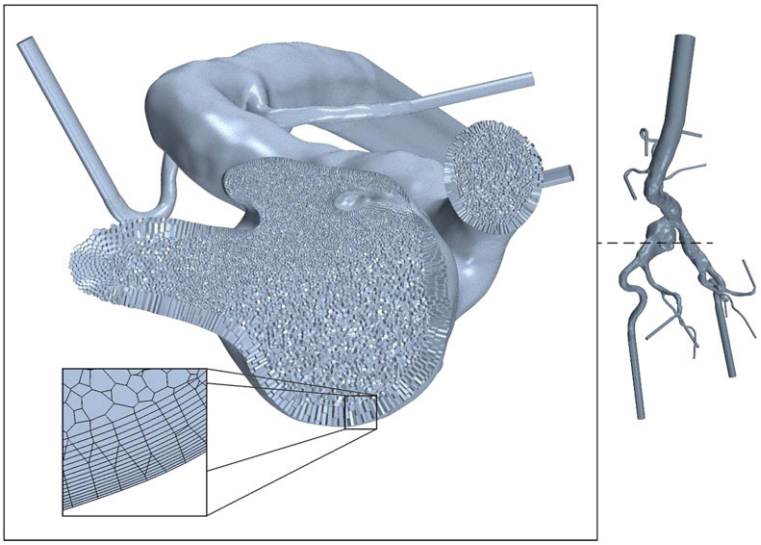

FIGURE 2 Mesh cross section through the common iliac artery aneurysm "pocket", highlighting the prism-layer mesh and local mesh refinement

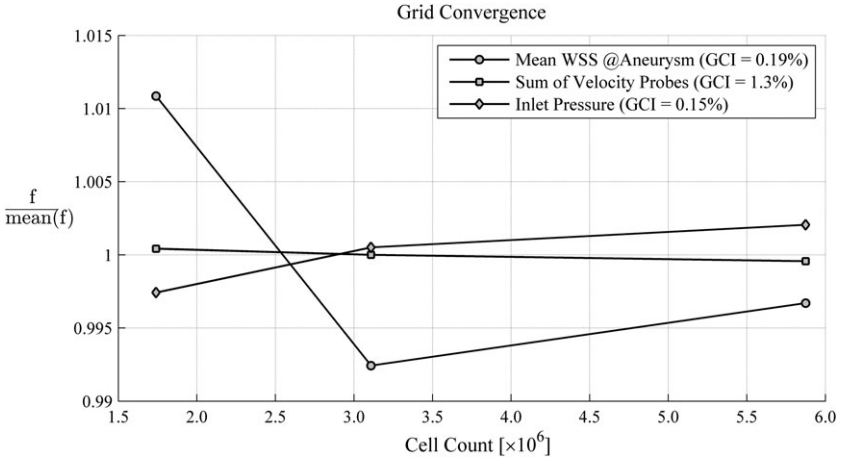

FIGURE 3 The normalized grid convergence of mean WSS across the common iliac artery, velocity probes, and inlet pressure plotted against the number of mesh-cells in the model domain. The results of the GCI calculations are included in the legend. GCI, Grid Convergence Index; WSS, wall shear stress

the arteries were characterized by no-slip, rigid wall boundary conditions[5,6,32,35,54,55] and the viscosity was modelled using a non-Newtonian approximation (Carreau-Yasuda, as implemented by Biasetti *et al*[44,56]). By using a non-Newtonian model, as opposed Newtonian, we can capture the macroscale shear-thinning of the blood, allowing a 1-way Lagrangian particle transport model to provide a good prediction of individual blood-cell trajectories within the continuous phase (blood). This methodology follows that of Basciano *et al* where the particle-particle and particle-fluid interactions are ignored[45] and is discussed further in Section 2.5.

For the inlet boundary condition (SC aorta), we applied a mass flow waveform derived from volumetric flow data by Les *et al*[57] (see Figure 4), where the waveform was scaled to suit the patient's age-estimated fat-free body mass using the allometric scaling relationships provided by Les *et al.*[57]

We explicitly coupled the 3D CFD simulation with a Windkessel model (RCR circuit) at each outlet boundary (see Figure 4) to be able to approximate the resistance and compliance of the downstream vascular beds. This improves the estimation of pressure throughout the domain and allows the pressure waveform at the SC inlet to comply with the patient's measured systolic and diastolic pressures.[57] Our Windkessel parameters are calibrated according to previous methodology,[35,58] with 30% of the common iliac flow passing through to the internal iliac artery. Furthermore, downstream of each internal iliac artery, the flow leaving the domain was split (directly) proportional to the area of each outlet boundary, and the shape of the flow waveform leaving each of the iliac outlets was configured to resemble the infrarenal (IR) aortic waveform. This occurs as the compliance values used at each outlet are proportionate to the mean flow, and a proximal to distal resistance ratio of 5.6%[58] is used at these outlets, similar to the study of Les et al.[35] These assumptions are necessary, as patient-specific flow and pressure data for each outlet were not collected. Figure 4 shows the calculated IR flow waveform and how it compares with the IR flow data from the study by Les *et al* (from which the inlet waveform was derived).[57]

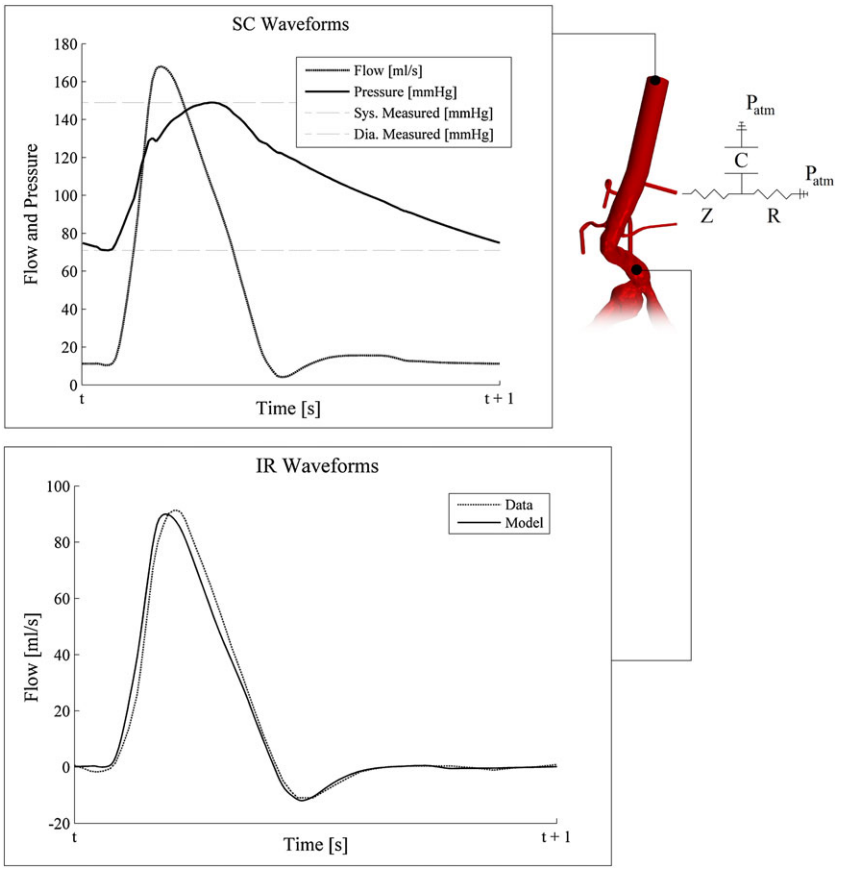

FIGURE 4 Top left: SC inlet waveforms and the patient's systolic and diastolic blood pressures. Top right: An example of the Windkessel model used at each outlet boundary, where Z is the proximal resistance, R is the distal resistance, and C is the vascular compliance. P_{atm} is atmospheric pressure. Bottom: IR flow waveforms—the modelled waveform closely matches the data of Les et al.[57] IR, infrarenal; SC, supraceliac

2.4 | TAWSS, OSI, and endothelial cell activation potential

The site specificity of thrombus distribution is compared with the TAWSS and OSI fields, as well as the endothelial cell activation potential (ECAP). The ECAP is the ratio between the OSI and TAWSS and is used to characterize the artery wall's degree of "thrombotic susceptibility" in 1 index.[36] We know from previous work that artery wall regions of TAWSS below 0.36 Pa expect monocyte/cell adhesion to occur[47,59–61] and the OSI describes maximum WSS vector oscillation, and atheroprone behavior, at a value of 0.5.[34,62] Considering this, the threshold of ECAP describing critical thrombotic susceptibility is inferred as regions close to and above 1.4 Pa^{-1}. The equations for TAWSS, OSI, and ECAP are

$$TAWSS = \frac{1}{T}\int_{t-T}^{t} |\boldsymbol{WSS}| dt, \tag{1}$$

$$OSI = \frac{1}{2}\left(1 - \frac{\left|\frac{1}{T}\int_{t-T}^{t} \boldsymbol{WSS} dt\right|}{\frac{1}{T}\int_{t-T}^{t} |\boldsymbol{WSS}| dt}\right), \tag{2}$$

$$ECAP = \frac{OSI}{TAWSS}, \tag{3}$$

where $\boldsymbol{WSS}$ is the instantaneous WSS vector, t is the instantaneous time, and T is the integration period (1 or more cardiac cycles).

We calculated the TAWSS and OSI for 100 intervals per cardiac cycle, and once the boundary waveforms converged (and any initial transience was not present), these results were computed for 10 cardiac cycles. Averaging for 10 cycles is conservative with most studies averaging fields over 3 or 5 cycles.[5,35,36] However, after the study by Poelma *et al,*[54] we investigated the convergence of these variables, as it had become clear that the systolic pulses were creating fluctuations within the CIAA that continued through diastole. When similar behavior was present in a model of Poelma *et al,*[54] they showed that 28 cycles of data did not lead to complete convergence at a particular location. However, in our study the convergence of the results was not so slow and a 10 cardiac cycle averaging was sufficient. Regarding the convergence of the TAWSS field across the CIAA, the relative error between a 10-cycle average and a 9-cycle average is 0.2%.

2.5 | One-way Lagrangian particle modelling

A 1-way Lagrangian methodology was used to model blood-cell trajectories through the iliac arteries. We injected platelets and monocytes into the flow field on a transverse-plane within the IR aorta, well upstream of the common iliac arteries (see Figure 5). We assumed these particles to be spherical with diameters of 2 and 16 μm and densities of 1040 and 1070 kg/m^3 for the platelets[45] and monocytes,[47] respectively. The particles were injected individually in parcels at randomly chosen spatial points (on the plane) with the same

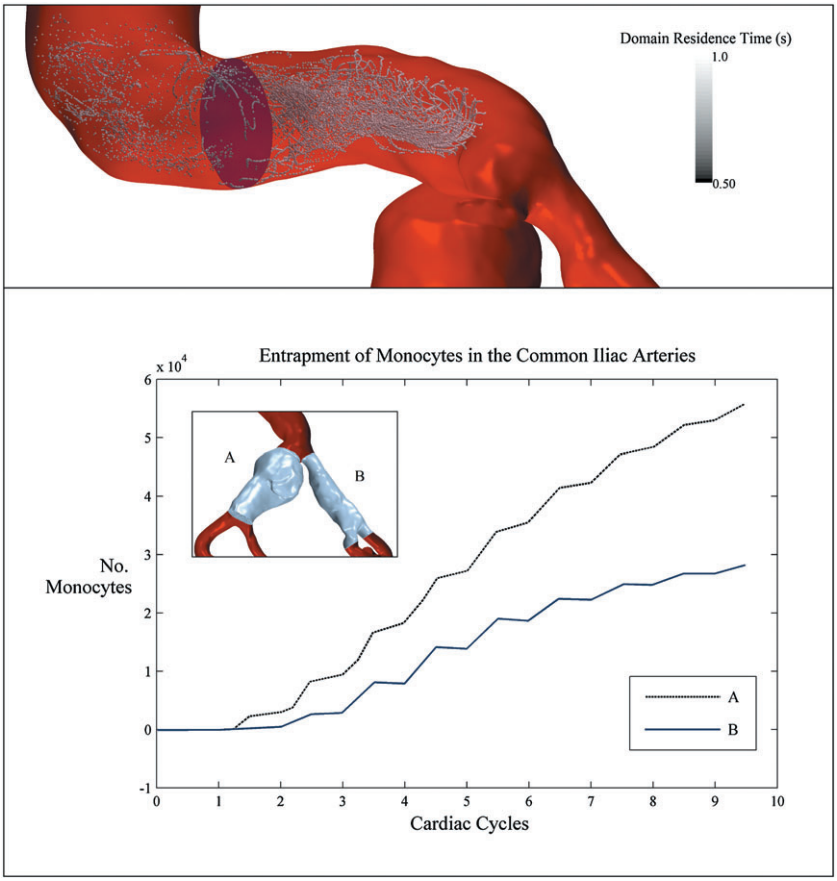

FIGURE 5 Top: Particles being injected for the first cycle in the infrarenal aorta. Bottom: Particle count in the common iliac arteries since injection

velocity as the continuous phase. The number of particles injected per time-step was proportional to the instantaneous mass flow through the IR aorta, and the forces acting on each particle were the pressure gradient force (Equation 4) and the drag force (Equation 5 and 6). Following the study of Basciano *et al*,[45] C_d (Equation 5) was the empirically derived Schiller-Naumann drag force coefficient, which varies for the transition between viscous and inertial particle transport.

$$F_d = \frac{1}{2} C_d \rho A_p |\boldsymbol{v_s}| \boldsymbol{v_s}, \tag{4}$$

$$C_d = \frac{Re_p}{24}\left(1 + 0.15 Re_p^{0.687}\right), \tag{5}$$

$$F_p = -V_p(\nabla P_s), \tag{6}$$

where Re_p is the particle Reynolds number, ρ is fluid density, $\boldsymbol{v_s}$ is the particle slip velocity, A_p is the projected particle area, V_p is particle volume, and ∇P_s is the gradient of static pressure.

Particle-wall collisions were considered linear-elastic, but with a wall adhesion probability (A_p) equal to the near-wall-PRT limiter (monocyte adhesion efficiency function) introduced by Hardman *et al*[47] (Equation 7):

$$A_p = \frac{(TAWSS - 0.4)^2}{2.4 TAWSS + 0.16}, \tag{7}$$

where the TAWSS must be less than 0.36 Pa for any wall adhesion to occur.

The particles were injected for 10 cardiac cycles, starting from a well-developed flow field (15 precomputed cycles), with 2×10^4 platelets and 2×10^4 monocytes injected per cycle. While the concentrations of both platelets and monocytes are not physically realistic, they are sufficient to test hypotheses of ILT formation.[45] The residence time of the particles is analyzed here using the residence time of the particles in the entire domain, rather than local sub-domains. Therefore, a particle's residence time is considered equivalent to the particle's age (and does not follow the more common assessments of residence time[63]). A cell-based residence time measures the minimum time spent by particles in the computational cells.[63] However, it was more computationally efficient (and effective) to view residence time as an average of particle age in each cell (possible due to the minimal-bias introduction of the particles upstream of each iliac artery). Henceforth, to be able to provide a comprehensive evaluation of how residence time varies throughout the geometry, for each of the modelled platelets and monocytes, we averaged the particle age at the nearest mesh-cell center for 40 evenly spaced time intervals spanning the final 2 cycles. This is referred to as mean domain residence time (DRT).

2.6 | Numerical solvers, simulation details, and particle trajectory validation

The Navier-Stokes equations were solved using STAR-CCM+'s finite-volume discretization and implicit-unsteady,

segregated flow solver. STAR-CCM+ implements a "SIMPLE algorithm" (Semi-Implicit Method for Pressure Linked Equations) when the flow is segregated to control the solution update and enforce mass conservation with each time-step.[64] We used the second-order upwind convection scheme and the temporal discretization was second order,[65] with 10^3 time-steps spanning each cardiac cycle and a minimum of 15 inner iterations per time-step. A convergence condition was implemented, requiring the convergence of the normalized[65] continuity and momentum residuals to remain below 10^{-3} ($\sim 10^{-9}$ absolute). However, additional inner iterations were seldom needed (only during the peak of the systolic phase).

We performed our simulations using all 12 central processing unit cores of a workstation with 2 Intel Xeon X5650 processors, and each cardiac cycle took approximately 24 to 48 hours, depending on the number of particles injected. The track file for the particle trajectories and monitored values reached 9 GB.

STAR-CCM+'s Lagrangian implicit-unsteady solver was used to evaluate the particle trajectories for each time-step. As the 1-way solution to the particle trajectories does not affect the Eulerian solution of the continuous phase, we only evaluated the particle trajectories at the last (Eulerian) iteration of each time-step. This unsteady approach follows the discrete element and discrete particle methods discussed in the study of Crowe *et al.*[66] The local time-steps used to march the particles are calculated dynamically so that the temporal error becomes negligible,[65] where these local time-steps are also bounded by minimum and maximum values. The first upper bound is the Eulerian time-step, and following this the maximum local time-steps are also bound by the momentum relaxation timescale used in the drag force model. Additionally, we imposed maximum and minimum Courant number (C) bounds, limiting the transport of particles (parcels) according to the characteristic length of each cell (Δx) and the maximum of the parcel ($\boldsymbol{v_p}$) or fluid ($\boldsymbol{v}$) velocity (Equation 8).

$$\frac{C_{\min}\,\Delta x}{\max\left(\left|\boldsymbol{v_p}\right|,\left|\boldsymbol{v}\right|\right)} \leq \delta t_p \leq \frac{C_{\max}\,\Delta x}{\max\left(\left|\boldsymbol{v_p}\right|,\left|\boldsymbol{v}\right|\right)}\ , \tag{8}$$

where $C_{\min} = 0.05$ and $C_{\max} = 0.35$.

To test the Lagrangian models, the particle trajectories and wall-deposition efficiency were investigated for a simple case: particle injection into steady flow through a 90° circular-pipe bend to model the physical experiments done by Pui *et al.*[67] Note, that because the flow was steady, after injection, the particles were marched until they were either deposited on the pipe wall or left the domain. The geometry and material/fluid properties used here follow that of Basciano *et al* for this case.[68] The diameter of these injected particles is varied and the wall-deposition efficiency is compared for different Stokes numbers (the ratio of the particle characteristic stopping distance to the vessel's characteristic length). We observed very good agreement with both the experimental work of Pui *et al* and the computational work of Basciano *et al.* For Stokes numbers spanning 0.04 to 0.6, the mean relative error between the modelled deposition efficiencies and the experimental values were 15% for our implementation and 93% for Basciano *et al.* However, when ignoring Stokes numbers below 0.1, both numerical models performed similarly (29% error).

3 | RESULTS AND DISCUSSION

3.1 | Particle residence and transport

As the injection location lay upstream of the common iliac arteries, it took 4 cycles for particles/cells to progress downstream of these arteries—half a cycle more on the side with the large aneurysm. The minimum time spent per particle within each common iliac artery was approximately 1 and a half cycles, and after 7 cycles each common iliac artery appeared densely populated with both monocytes and platelets. As shown in Figure 5, the net influx of particles continued to grow for both common iliac arteries, and by the tenth cycle, the left side artery with the large aneurysm harbored approximately 6×10^4 monocytes and 6×10^4 platelets. In contrast, the other common iliac artery had half as many particles enter; however, it managed to entrap a similar portion of these particles. Regarding this, the ratio of maximum diameter to inlet diameter for both common iliac arteries is similar, at approximately 1.9. However, the inlet to the left CIAA is much greater than the inlet to the other common iliac artery and has a vortex spanning its entrance (discussed later; see Figure 8). This vortex is possibly assisting the greater particle transport into the large aneurysm.

We observed little difference between the monocyte and platelet trajectories. Because of their small physical sizes, both cell-types have low momentum response times and respond promptly to changes in the flow field. The suspension of monocytes and platelets occurred in both common iliac arteries (upon the particle slip velocity reaching 0). When this happens there is no difference in the immediate residence of either cell-type at a particular location, as they both follow the carrier fluid. In addition, a negligible amount of cell adhesion occurred throughout the model.

In the left CIAA, the mean DRT of both monocytes and platelets was elevated near the wall in the regions of significant ILT formation (almost everywhere). As shown in Figure 6, the lower and/or anterior portion of the aneurysm sac where the most ILT forms is associated with a large region of high mean DRT and cell entrapment. Another primary observation is the complete entrapment of cells within the pocket on the anterior side of the aneurysm (highest mean DRT).

There was reasonable agreement between the mean DRT and ILT location in the right contralateral common iliac artery (see Figure 7). We observed the posterior side near

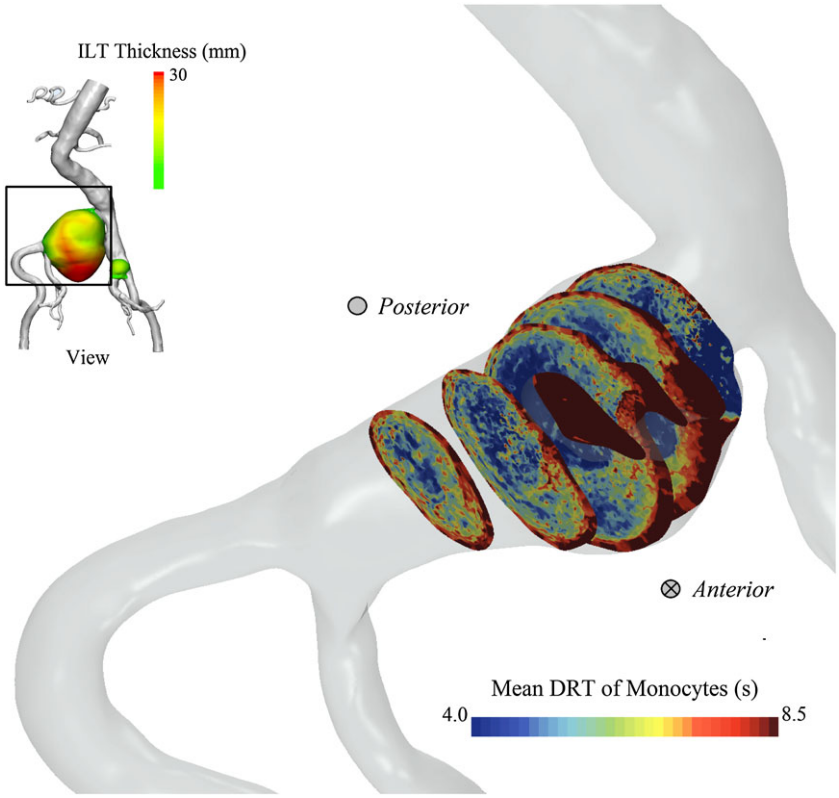

FIGURE 6 Plane sections showing the mean DRT of monocytes within the large left common iliac artery aneurysm and color-coded intraluminal thrombus thickness (top left). DRT, domain residence time

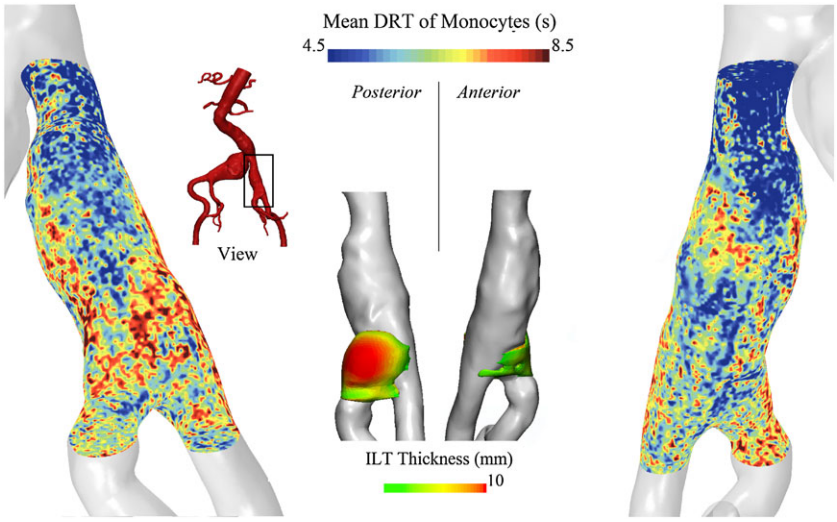

FIGURE 7 Posterior and anterior views of intraluminal thrombus and mean DRT in the less-diseased common iliac artery. This is a volume-rendering of mean DRT showing the field value in the surface-adjacent mesh-cell—which well represents the internal distribution of mean DRT in the fluid boundary layer. DRT, domain residence time

the distal bifurcation to have the greatest amount of ILT present and high mean DRT. However, we also found the exterior of the posterior side to have high mean DRT and cell entrapment, despite having no localized ILT formation. The mean DRT on the anterior side is more diffuse, with less ILT observed on CT. Our findings also show that the mean DRT is higher in regions where the artery is locally expanding—with some high mean DRT in the upstream, despite an absence of ILT. Future ILT formation may be expected in these regions; however, the absence of follow-up data means that, in this instance, these regions show disagreement with expectations of ILT specificity.

3.2 | Velocity fields

We found clear differences in the velocity fields between the 2 arteries, which can be attributed to the geometric differences. In the left CIAA, the inlet/neck angle to the upstream aorta is only slightly greater than that of the other common iliac, yet the inlet diameter is much greater (~2×). We observed a vortex structure moving across the entrance to the left CIAA, which formed during systole at a point of flow separation on the top lip (see Figure 8A). This vortex structure leaves the aneurysm entrance and travels downward toward the anterior region of the aneurysm sac where it disperses when the net direction of flow reverses. Similar to

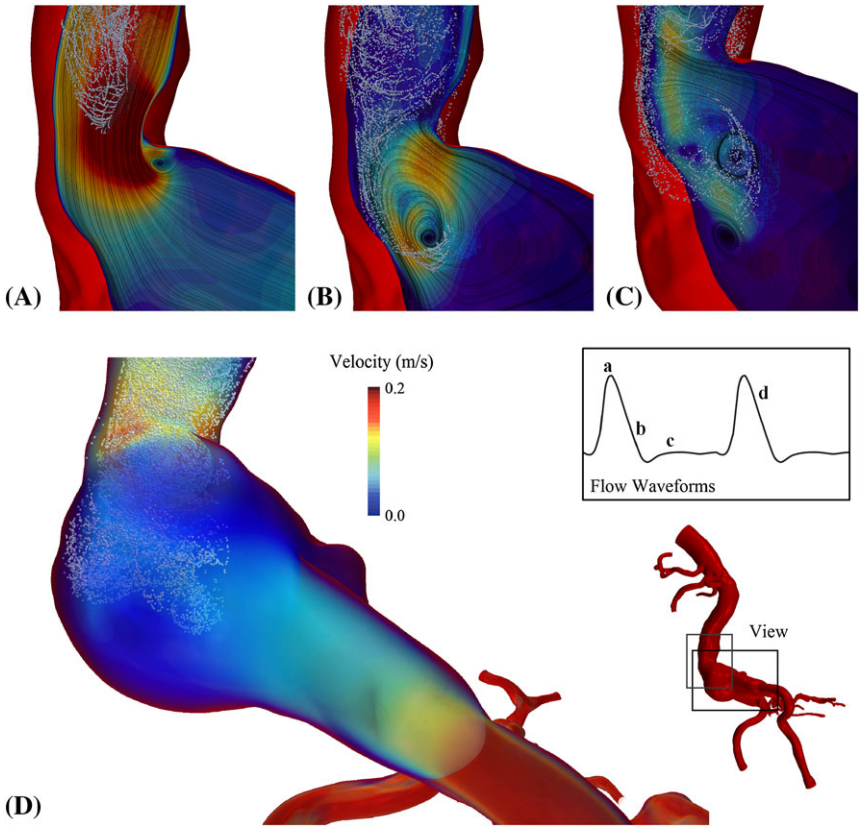

FIGURE 8 Platelets entering the left common iliac artery aneurysm for 4 time points (A, B, C, and D) within the second and third cardiac cycles (since particle injection). Images A, B, and C show plane-constrained velocity streamlines through the aneurysm neck, while image D shows a volume-rendering of the velocity field. This figure highlights the production of a vortex at the inlet to the aneurysm during systole (images A and B) and how this structure progresses toward the lower portion of the aneurysm during diastole, ultimately diverting entering particles toward the aneurysms lower, heavily intraluminal thrombus–burdened region. This behavior is similar to the previous hypothesis on the formation of intraluminal thrombus in aortic aneurysms (because of the observed vortex transport)[40]

the postulation by Biasetti *et al*,[40] this structure, which meets the λ_2 criterion of a vortex,[69] carries with it many of the platelets and monocytes into the lower/anterior regions of the aneurysm sac where the majority of ILT has formed (see Figure 8). This behavior occurs because of the low Stokes number of the particles: they lack the inertia necessary to leave or travel unaffected by coherent vortices. In this CIAA, we also found a permanent stagnation of flow within the pocket on the posterior side and extremely low flow in the anterior region of the aneurysm sac. These regions, which are the most diseased/abnormal, are not flushed out during systolic flow. Furthermore, while the particles migrate to these regions of low flow, it takes longer for them to get close to the walls as they encounter significant deceleration. It required 10 cycles for the concentration of platelets and monocytes within 1 cm of the aneurysm's lower anterior surface (9.5% of aneurysm volume) to reach the average concentration within the aneurysm. The flow stagnation and associated low TAWSS in this region lead to a high wall-cell adhesion probability. However, the inability for particles to reach the wall results in a negligible amount of wall-cell adhesion occurring in this model.

Figure 9 shows the key stages of the velocity field within the right common iliac artery. Over the course of the cardiac cycle significant rotary motion in the free stream only occurred during late diastole, after flow reversal. The flow completely realigned itself during the systolic phase and sees an efficient transport of blood distally during this period. During systole, vortices formed where the artery begins to dilate at the proximal end. While these vortices did not exist for all phases of the cardiac cycle, as they progressed downstream they appeared to encourage particle transport toward the wall. There were a number of low-velocity recirculation zones that were well developed at the end of systole near the regions where the ILT has formed in the distal of the artery (see Figure 9C and D).

3.3 | Wall shear stress fields and thrombus susceptibility

We found extremely low TAWSS (expected cell adhesion) and a high OSI across the large aneurysm, in particular, within the "pocket" (see Figure 10). There were large differences in both the TAWSS and OSI fields on the upper/posterior and lower/anterior surfaces of the aneurysm, correlating with regions of ILT. This is represented clearly by the ECAP, as the majority of mesh-cell faces on the lower/anterior surface are above the estimated value for critical thrombus susceptibility (1.4 Pa^{-1}). Furthermore, the aneurysm's pocket, for all indices, was found to be the most thrombus susceptible region, as it sees the largest ECAP as well as the largest mean DRT, and flow stagnation. However, bulk transport of platelets and monocytes to that region did not occur, as most of the modelled particles more readily resided in other regions of the aneurysm where the flow was less stagnant, though still providing the necessary conditions for entrapment, ie, in the lower/anterior of the sac. This may explain the lack of more

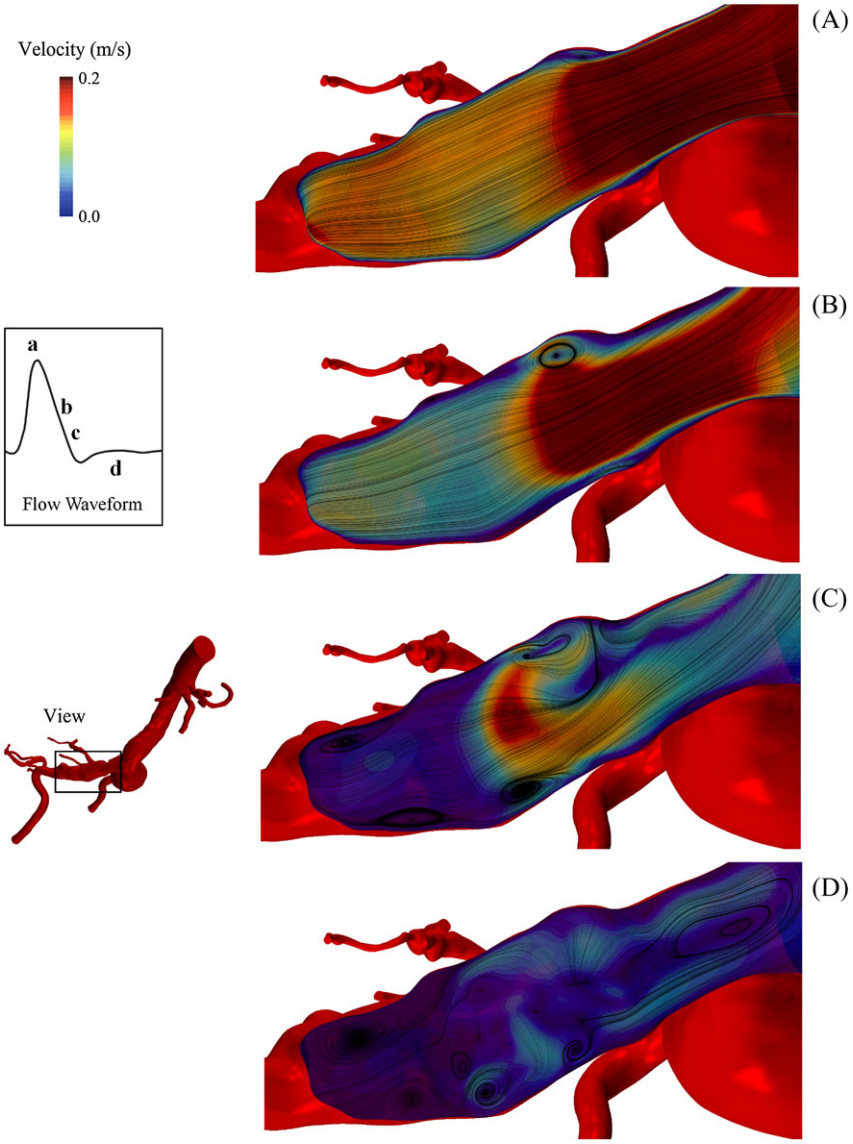

FIGURE 9 The plane tangential velocity field with constrained streamlines in center of the less-diseased common iliac artery for 4 time points (A, B, C, and D). Image A shows the velocity field during the systolic phase. Image B shows the velocity field during systolic deceleration and the development of a vortex where the artery begins to dilate. Image C shows the end of the systolic phase and the development of low-velocity vortices near the distal bifurcation. Image D shows the velocity field as the net transport of blood through the artery reaches 0

significant thrombus close to the pocket (ILT thickness is ~10 mm near the pocket).

In the other common iliac artery, the ECAP field showed some agreement with the site specificity of ILT (see Figure 11). The region near the bifurcation experienced low enough WSS for expected cell adhesion, and we found a large patch of high OSI on the posterior surface of the artery where the majority of ILT formed. However, in the proximal region of this artery, where no ILT developed, there were some similar trends in the WSS fields (and some aneurysmal development). Although the absence of low-velocity, high-residence time recirculation zones in the upstream may explain why ILT formed in the distal portion of the artery, which would agree with the previous hypothesis of ILT formation in the distal sac.[40]

Our results would be more conclusive, and less subjective, if baseline and/or follow-up data were available for analysis. Although it remains clear that the CIAAs in this patient present similar values for the hemodynamic metrics at the locations of thrombotic built-up, being proportional to the amount of thrombus developed in these regions.

4 | LIMITATIONS

First, we have only investigated 1 case and we need to extend our study to include more patients with different geometric variations. Notably, the lack of any healthier, baseline data limits the interpretation of the results. Second, regarding the physics of our simulation, without a near-wall lift force,[46,47] the transport of particles away from (and toward) the wall may be lacking, and some of the particles could become artificially stuck in the near-wall boundary layer. However, as it took a long time for particles to penetrate into lower velocity regions, when considering ILT-associated flow stagnation (and particle suspension), wall-particle interaction may be reasonably expected, and therefore, a superior near-wall

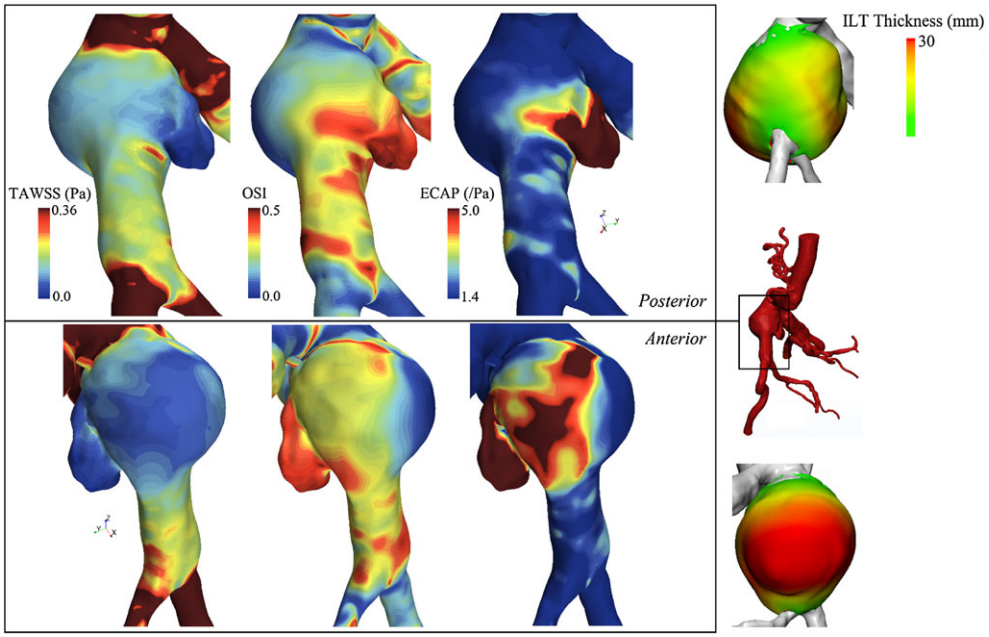

FIGURE 10 TAWSS, OSI, and ECAP fields shown for both the posterior/top and anterior/bottom of the common iliac artery with the large aneurysm. ECAP, endothelial cell activation potential; ILT, intraluminal thrombus; TAWSS, time-averaged wall shear stress; OSI, oscillatory shear index

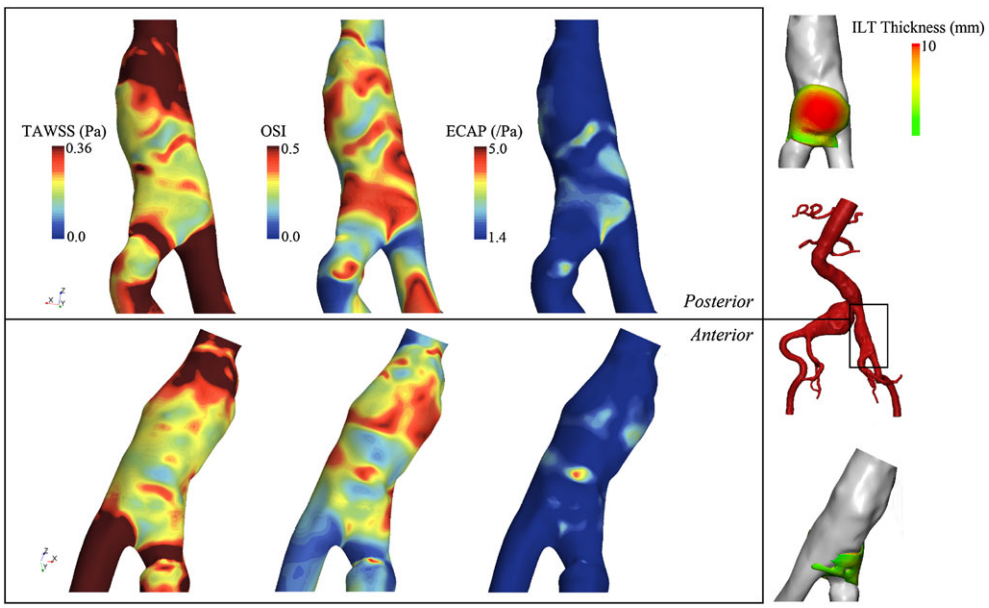

FIGURE 11 TAWSS, OSI, and ECAP fields shown for both the posterior and anterior of the less-diseased common iliac artery. ECAP, endothelial cell activation potential; ILT, intraluminal thrombus; TAWSS, time-averaged wall shear stress; OSI, oscillatory shear index

model may simply confirm these expectations. The physical models used here lack the chemical cues and blood cell-to-wall recruitment mechanisms that are present, *in vivo*.

The time frame over which the results are gathered strongly affects observed particle behavior and the measured residence times. Ten cycles of data may not be sufficient to gain a proper understanding of particle transport in larger aneurysms. However, residence time information may be gained with more computational ease if the particles were seeded within the areas of interest, or by considering fluid residence through the transport of a passive scalar—in the absence of particle modelling. Nevertheless, the particle modelling approach we used here remains a promising way to understand, develop, and test hypotheses about ILT formation in aneurysms. A more comprehensive representation of PRT may be implemented using existing cell-based methods[63]—requiring a greater concentration of particles to be able to (accurately) measure the time spent by particles in each computational cell (ie, mean exposure time[63,70]).

The ECAP and associated WSS fields are limited as they only provide a measurement of thrombotic susceptibility, and further information about the flow field and particle history

remains critical to the analysis of ILT formation. The methodology used in this study to assess the site specificity of ILT may be simplified. The recent work of Di Achille *et al*[36] further scales the ECAP by the platelet activation potential recently proposed by Shadden and Hendabadi[71] to calculate a new thrombus formation potential. By combining information on the flow-induced shear history of wall-proximal platelets with information on the thrombotic susceptibility (ECAP) of the endothelial layer, a single, simple measure can be produced.

5 | CONCLUSION

We examined the residence of monocytes and platelets within a patient's 2 common iliac arteries. As there are 2 common iliac arteries, when they have different levels of aneurysmal dilation and ILT burden, there is an excellent opportunity to compare and contrast the hemodynamic stimuli associated with this disease. This type of comparison cannot be done when solely studying AAA. Because of this, further study of the hemodynamics in the common iliac arteries has the potential to improve our understanding of aneurysm growth and ILT development.

We have presented a comprehensive method of simulating particle dispersion and have correlated residence of particles to the site of ILT. We also compared regions of ILT to the behavior of the velocity field, TAWSS, OSI, and ECAP. We have shown that high residence time, flow stagnation, vortex transport, and high ECAP all correlate spatially with the regions where ILT developed. This trend was observed in the patient's left CIAA and can be seen as an emerging trend in the contralateral common iliac artery. Our findings show some support for the previous hypotheses of thrombus formation[40] and convey that, in this case at least, the hemodynamic indicators correlated with regions of thrombus buildup, as well as the sustained development and growth of the thrombus. However, these conclusions would be more substantive if baseline and/or follow-up data were available to confirm them.

ACKNOWLEDGMENTS

We would like to sincerely thank CD-adapco for their generous support of our research. We would like to also thank the National Health and Medical Research Council (grants APP1063986 and APP1083572), as well as the Australia Postgraduate Award and the ISML Computational Biomechanics for Medicine scholarship.

ABBREVIATIONS USED

CIAA	common iliac artery aneurysm
AAA	abdominal aortic aneurysm
CFD	computational fluid dynamics
CT	computed tomography
ILT	intraluminal thrombus
WSS	wall shear stress
TAWSS	time-averaged wall shear stress
OSI	oscillatory shear index
PRT	particle residence time
3D	3-dimensional
SC	supraceliac
GCI	Grid Convergence Index
IR	infrarenal
ECAP	endothelial cell activation potential
DRT	domain residence time

REFERENCES

1. Svensjö S, Björck M, Gürtelschmid M, et al. Low prevalence of abdominal aortic aneurysm among 65-year-old Swedish men indicates a change in the epidemiology of the disease. *Circulation*. 2011;124(10):1118–1123. doi: 10.1161/circulationaha.111.030379
2. Norman PE, Lawrence-Brown M, Semmens J, et al. The anatomical distribution of iliac aneurysms: is there an embryological basis? *Eur J Vasc Endovasc Surg.* 2003;25(1):82–84. doi: 10.1053/ejvs.2002.1780
3. Norman PE, Powell JT. Site specificity of aneurysmal disease. *Circulation*. 2010;121(4):560–568. doi: 10.1161/CIRCULATIONAHA.109.880724
4. Huang Y, Gloviczki P, Duncan AA, et al. Common iliac artery aneurysm: expansion rate and results of open surgical and endovascular repair. *J Vasc Surg.* 2008;47(6):1203–1210. doi: 10.1016/j.jvs.2008.01.050
5. Doyle BJ, McGloughlin TM, Kavanagh EG, et al. From Detection to Rupture: A Serial Computational Fluid Dynamics Case Study of a Rapidly Expanding, Patient-Specific, Ruptured Abdominal Aortic Aneurysm. In: *Computational Biomechanics for Medicine*. New York: Springer;2014:53–68.
6. Steinman DA, Hoi Y, Fahy P, et al. Variability of computational fluid dynamics solutions for pressure and flow in a giant aneurysm: the ASME 2012 Summer Bioengineering Conference CFD Challenge. *J Biomech Eng.* 2013;135(2):021016. doi: 10.1115/1.4023382
7. Tong J, Holzapfel GA. Structure, mechanics, and histology of intraluminal thrombi in abdominal aortic aneurysms. *Ann Biomed Eng.* 2015;43(7):1488–1501. doi: 10.1007/s10439-015-1332-5
8. Sun Z, Xu L. Computational fluid dynamics in coronary artery disease. *Comput Med Imaging Graph.* 2014;38(8):651–663. doi: 10.1016/j.compmedimag.2014.09.002
9. Doyle BJ, Callanan A, Burke PE, et al. Vessel asymmetry as an additional diagnostic tool in the assessment of abdominal aortic aneurysms. *J Vasc Surg.* 2009;49(2):443–454. doi: 10.1016/j.jvs.2008.08.064
10. Doyle BJ, McGloughlin TM, Miller K, et al. Regions of high wall stress can predict the future location of rupture of abdominal aortic aneurysm. *Cardiovasc Intervent Radiol.* 2014;37(3):815–818. doi: 10.1007/s00270-014-0864-7
11. Gasser TC, Auer M, Labruto F, et al. Biomechanical rupture risk assessment of abdominal aortic aneurysms: model complexity versus predictability of finite element simulations. *Eur J Vasc Endovasc Surg.* 2010;40(2):176–185. doi: 10.1016/j.ejvs.2010.04.003
12. Pijls NHJ, de Bruyne B, Peels K, et al. Measurement of fractional flow reserve to assess the functional severity of coronary-artery stenoses. *N Engl J Med.* 1996;334(26):1703–1708. doi: 10.1056/NEJM199606273342604
13. Tonino PAL, de Bruyne B, Pijls NH, et al. Fractional flow reserve versus angiography for guiding percutaneous coronary intervention. *N Engl J Med.* 2009;360(3):213–224. doi: 10.1056/NEJMoa0807611
14. Blacher J, Asmar R, Djane S, et al. Aortic pulse wave velocity as a marker of cardiovascular risk in hypertensive patients. *Hypertension*. 1999;33(5):1111–1117. doi: 10.1161/01.hyp.33.5.1111
15. Wilkinson IB, Cockcroft JR, Webb DJ. Pulse wave analysis and arterial stiffness. *J Cardiovasc Pharmacol.* 1998;32(Suppl 3):S33–S37.

16. Arzani A, Shadden SC. Characterization of the transport topology in patient-specific abdominal aortic aneurysm models. *Phys Fluids.* 2012;24(8) 081901. doi: 10.1063/1.4744984

17. Sabooni H, Hassani K, Bahraseman HG. Modeling of iliac artery aneurysm using fluid-structure interaction. *J. Mech. Med. Biol.*. 2015;15(01) 1550041. doi: 10.1142/S0219519415500414

18. Harter LP, Gross BH, Callen PW, et al. Ultrasonic evaluation of abdominal aortic thrombus. *J Ultrasound Med.* 1982;1(8):315–318.

19. Houard X, Rouzet F, Touat Z, et al. Topology of the fibrinolytic system within the mural thrombus of human abdominal aortic aneurysms. *J Pathol.* 2007;212(1):20–28. doi: 10.1002/path.2148

20. Swedenborg J, Eriksson P. The intraluminal thrombus as a source of proteolytic activity. *Ann N Y Acad Sci.* 2006;1085:133–138. doi: 10.1196/annals.1383.044

21. Vande Geest JP, Wang DH, Wisniewski SR, et al. Towards a noninvasive method for determination of patient-specific wall strength distribution in abdominal aortic aneurysms. *Ann Biomed Eng*. 2006;34(7):1098–1106. doi: 10.1007/s10439-006-9132-6

22. Speelman L, Schurink GW, Bosboom EM, et al. The mechanical role of thrombus on the growth rate of an abdominal aortic aneurysm. *J Vasc Surg.* 2010;51(1):19–26. doi: 10.1016/j.jvs.2009.08.075

23. Hans SS, Jareunpoon O, Balasubramaniam M, *et al*. Size and location of thrombus in intact and ruptured abdominal aortic aneurysms. *J Vasc Surg.* 2005;41(4):584–588. doi: 10.1016/j.jvs.2005.01.004

24. Truijers M, Fillinger MF, Renema KW, et al. *In-vivo* imaging of changes in abdominal aortic aneurysm thrombus volume during the cardiac cycle. *J Endovasc Ther.* 2009;16(3):314–319. doi: 10.1583/08-2625.1

25. O'Leary SA, Kavanagh EG, Grace PA, et al. The biaxial mechanical behaviour of abdominal aortic aneurysm intraluminal thrombus: classification of morphology and the determination of layer and region specific properties. *J Biomech.* 2014;47(6):1430–1437. doi: 10.1016/j.jbiomech.2014.01.041

26. Labruto F, Blomqvist L, Swedenborg J. Imaging the intraluminal thrombus of abdominal aortic aneurysms: techniques, findings, and clinical implications. *J Vasc Interv Radiol.* 2011;22(8):1069–1075. doi: 10.1016/j.jvir.2011.01.454

27. Salsac AV, Sparks S, Lasheras J. Hemodynamic changes occurring during the progressive enlargement of abdominal aortic aneurysms. *Ann Vasc Surg.* 2004;18(1):14–21. doi: 10.1007/s10016-003-0101-3

28. Salsac AV, Sparks SR, Chomaz JM, et al. Evolution of the wall shear stresses during the progressive enlargement of symmetric abdominal aortic aneurysms. *J Fluid Mech.* 2006;560:19–51. doi: 10.1017/S002211200600036X

29. Lasheras JC. The biomechanics of arterial aneurysms. *Ann Rev Fluid Mech* 2007;39(1):293–319. doi: 10.1146/annurev.fluid.39.050905.110128

30. Raz S, Einav S, Alemu Y, et al. DPIV prediction of flow induced platelet activation—comparison to numerical predictions. *Ann Biomed Eng.* 2007;35(4):493–504. doi: 10.1007/s10439-007-9257-2

31. Rayz VL, Boussel L, Ge L, et al. Flow residence time and regions of intraluminal thrombus deposition in intracranial aneurysms. *Ann Biomed Eng.* 2010;38(10):3058–3069. doi: 10.1007/s10439-010-0065-8

32. Boyd AJ, Kuhn DC, Lozowy RJ, et al. Low wall shear stress predominates at sites of abdominal aortic aneurysm rupture. *J Vasc Surg.* 2015;7. doi: 10.1016/j.jvs.2015.01.040

33. Lehoux S, Castier Y, Tedgui A. Molecular mechanisms of the vascular responses to haemodynamic forces. *J Intern Med.* 2006;259(4):381–392. doi: 10.1111/j.1365-2796.2006.01624.x

34. Ku DN, Giddens DP, Zarins CK, et al. Pulsatile flow and atherosclerosis in the human carotid bifurcation. Positive correlation between plaque location and low oscillating shear stress. *Arterioscler Thromb Vasc Biol.* 1985;5(3):293–302. doi: 10.1161/01.atv.5.3.293

35. Les AS, Shadden SC, Figueroa CA, et al. Quantification of hemodynamics in abdominal aortic aneurysms during rest and exercise using magnetic resonance imaging and computational fluid dynamics. *Ann Biomed Eng.* 2010;38(4):1288–1313. doi: 10.1007/s10439-010-9949-x

36. Di Achille P, Tellides G, Figueroa CA, et al. A haemodynamic predictor of intraluminal thrombus formation in abdominal aortic aneurysms. *Proc R Soc A Math Phys Eng Sci.* 2014;470(2172) 20140163. doi: 10.1098/rspa.2014.0163

37. O'Rourke MJ, McCullough JP, Kelly S. An investigation of the relationship between hemodynamics and thrombus deposition within patient-specific models of abdominal aortic aneurysm. *Proc Inst Mech Eng H.* 2012;226(7):548–564.

38. Arzani A, Suh GY, Dalman RL, et al. A longitudinal comparison of hemodynamics and intraluminal thrombus deposition in abdominal aortic aneurysms. *Am J Physiol Heart Circ Physiol.* 2014;307(12):H1786–H1795. doi: 10.1152/ajpheart.00461.2014

39. Yamazumi K, Ojiro M, Okumura H, *et al*. An activated state of blood coagulation and fibrinolysis in patients with abdominal aortic aneurysm. *Am J Surg.* 1998;175(4):297–301. doi: 10.1016/S0002-9610(98)00014-2

40. Biasetti J, Hussain F, Gasser TC. Blood flow and coherent vortices in the normal and aneurysmatic aortas: a fluid dynamical approach to intra-luminal thrombus formation. *J R Soc Interface.* 2011;8(63):1449–1461. doi: 10.1098/rsif.2011.0041

41. Guimaraes TA, Garcia GN, Dalio MB, et al. Morphological aspects of mural thrombi deposition residual lumen route in infrarenal abdominal aorta aneurisms. *Acta Cir Bras.* 2008;23(Suppl 1):151–156. discussion 156

42. Muraki N. Ultrasonic studies of the abdominal aorta with special reference to hemodynamic considerations on thrombus formation in the abdominal aortic aneurysm. *J Jap Coll Angiol.* 1983;23:401–413.

43. de Ceniga MV, Gómez R, Estallo L, et al. Analysis of expansion patterns in 4-4.9 cm abdominal aortic aneurysms. *Ann Vasc Surg.* 2008;22(1):37–44. doi: 10.1016/j.avsg.2007.07.036

44. Biasetti J, Spazzini PG, Swedenborg J, et al. An integrated fluid-chemical model toward modeling the formation of intra-luminal thrombus in abdominal aortic aneurysms. *Front Physiol.* 2012;3:266. doi: 10.3389/fphys.2012.00266

45. Basciano C, Kleinstreuer C, Hyun S, et al. A relation between near-wall particle-hemodynamics and onset of thrombus formation in abdominal aortic aneurysms. *Ann Biomed Eng.* 2011;39(7):2010–2026. doi: 10.1007/s10439-011-0285-6

46. Longest PW, Kleinstreuer C, Buchanan JR. Efficient computation of micro-particle dynamics including wall effects. *Comput Fluids.* 2004;33(4):577–601. doi: 10.1016/j.compfluid.2003.06.002

47. Hardman D, Doyle BJ, Semple SI, et al. On the prediction of monocyte deposition in abdominal aortic aneurysms using computational fluid dynamics. *Proc Inst Mech Eng H.* 2013;227(10):1114–1124. doi: 10.1177/0954411913494319

48. Wood NB. Aspects of fluid dynamics applied to the larger arteries. *J Theor Biol.* 1999;199(2):137–161. doi: 10.1006/jtbi.1999.0953

49. Kelsey LK, Miller K, Norman PE, et al. The influence of downstream branching arteries on upstream haemodynamics. *J Biomech*. 2016. doi:10.1016/j.biomech.2016.07.023

50. Roache PJ. Perspective: a method for uniform reporting of grid refinement studies. *J Fluids Eng.* 1994;116(3):405–413. doi: 10.1115/1.2910291

51. Celik IB, Ghia U, Roache PJ, et al. Procedure for estimation and reporting of uncertainty due to discretization in CFD applications. *J Fluids Eng.* 2008;130(7):078001–078001. doi: 10.1115/1.2960953

52. Taylor C, Steinman D. Image-based modeling of blood flow and vessel wall dynamics: applications, methods and future directions. *Ann Biomed Eng.* 2010;38(3):1188–1203. doi: 10.1007/s10439-010-9901-0

53. Stonebridge PA, Brophy CM. Spiral laminar flow in arteries? *Lancet.* 1991;338(8779):1360–1361. doi: 10.1016/0140-6736(91)92238-W

54. Poelma C, Watton PN, Ventikos Y. Transitional flow in aneurysms and the computation of haemodynamic parameters. *J R Soc Interface*. 2015;12(105). doi: 10.1098/rsif.2014.1394

55. Wolters BJBM, Rutten MC, Schurink GW, et al. A patient-specific computational model of fluid–structure interaction in abdominal aortic aneurysms. *Med Eng Phys.* 2005;27(10):871–883. doi: 10.1016/j.medengphy.2005.06.008

56. Leuprecht A, Perktold K. Computer simulation of non-Newtonian effects on blood flow in large arteries. *Comput Methods Biomech Biomed Engin.* 2001;4(2):149–163. doi: 10.1080/10255840008908002

57. Les AS, Yeung JJ, Schultz GM, et al. Supraceliac and infrarenal aortic flow in patients with abdominal aortic aneurysms: mean flows, waveforms, and allometric scaling relationships. *Cardiovasc Eng Technol.* 2010;1(1). doi: 10.1007/s13239-010-0004-8
58. Laskey WK, Parker HG, Ferrari VA, et al. Estimation of total systemic arterial compliance in humans. *J Appl Physiol (Bethesda, Md. : 1985)* 1990;69 (1):112–119.
59. Lawrence MB, Berg EL, Butcher EC, et al. Rolling of lymphocytes and neutrophils on peripheral node addressin and subsequent arrest on ICAM-1 in shear flow. *Eur J Immunol.* 1995;25(4):1025–1031. doi: 10.1002/eji.1830250425
60. Lawrence MB, McIntire LV, Eskin SG. Effect of flow on polymorphonuclear leukocyte/endothelial cell adhesion. *Blood*. 1987;70(5):1284–1290.
61. Worthen GS, Smedly LA, Tonnesen MG, et al. Effects of shear stress on adhesive interaction between neutrophils and cultured endothelial cells. *J Appl Physiol (Bethesda, Md. : 1985)*. 1987;63(5):2031–2041.
62. Ku DN, Glagov S, Moore JE Jr, et al. Flow patterns in the abdominal aorta under simulated postprandial and exercise conditions: an experimental study. *J Vasc Surg.* 1989;9(2):309–316. doi: 10.1016/0741-5214(89)90051-7
63. Shadden SC, Arzani A. Lagrangian postprocessing of computational hemodynamics. *Ann Biomed Eng.* 2015;43(1):41–58. doi: 10.1007/s10439-014-1070-0
64. Fergizer JH, Peric M. *Comput. Meth. Fluid Dynam*. 3 ed. Berlin-Heidelberg: Springer; 2002.
65. CD-adapco. STAR-CCM+ User Guide. 2014.
66. Crowe CT, Schwarzkopf JD, Sommerfeld M, et al. Droplet-Particle Cloud Equations. In: *Multiphase Flows with Droplets and Particles*. 2nd ed. Boca Raton, FL: CRC Press; 2011: 235–258. doi: 10.1201/b11103-9
67. Pui DYH, Romay-Novas F, Liu BYH. Experimental study of particle deposition in bends of circular cross section. *Aerosol Sci Tech.* 1987;7(3):301–315. doi: 10.1080/02786828708959166
68. Basciano C. Computational particle-hemodynamics analysis applied to an abdominal aortic aneurysm with thrombus and microsphere-targeting of liver tumors. In: *Department of Mechanical and Aerospace Engineering*. Raleigh, NC: North Carolina State University; 2010.
69. Jeong J, Hussain F. On the identification of a vortex. *J Fluid Mech.* 1995;285:69–94. doi: 10.1017/S0022112095000462
70. Lonyai A, Dubin AM, Feinstein JA, et al. New insights into pacemaker lead-induced venous occlusion: simulation-based investigation of alterations in venous biomechanics. *Cardiovasc Eng.* 2010;10(2):84–90. doi: 10.1007/s10558-010-9096-x
71. Shadden S, Hendabadi S. Potential fluid mechanic pathways of platelet activation. *Biomech Model Mechanobiol.* 2013;12(3):467–474. doi: 10.1007/s10237-012-0417-4
72. Human Gross Anatomy Atlas. Available from: http://cias.rit.edu/~tpf1471/Fitzgerald_783/anatomy/pelvisSkeleton.html. [1 May 2015].

How to cite this article: Kelsey LJ, Powell JT, Norman PE, Miller K, Doyle BJ. A comparison of hemodynamic metrics and intraluminal thrombus burden in a common iliac artery aneurysm. *Int J Numer Meth Biomed Engng*. 2017;33:e2821. https://doi.org/10.1002/cnm.2821